Seasonal and hemispheric asymmetries in the cold ion outflow source region: Swarm and CHAMP observations of F-region polar cap plasma density

Spencer Mark Hatch[1], Stein Haaland[1], Karl M. Laundal[2], Therese Moretto Jorgensen[3], Andrew Yau[4], Lindis Merete Bjoland[5], Jone Peter Reistad[6], Anders Ohma[6], and Kjellmar Oksavik[2]

[1]Birkeland Centre for Space Science
[2]University of Bergen
[3]UNIVERSITY OF BERGEN
[4]University of Calgary
[5]The University Centre in Svalbard
[6]Birkeland Centre for Space Science, University of Bergen

November 30, 2022

Abstract

One of the primary mechanisms of loss of Earth's atmosphere is the persistent "cold" ([?] 20 eV) ion outflow that has been observed in the magnetospheric lobes over large volumes with dimensions of order several Earth radii (R). As the main source of this cold ion outflow, the polar cap -region ionosphere and conditions within it have a disproportionate influence on these magnetospheric regions. Using 15 years of measurements of plasma density N made by the Swarm spacecraft constellation and the CHAMP spacecraft within the region of the polar cap above 80{degree sign} Apex magnetic latitude, we report evidence of several types of seasonal asymmetries in polar cap N. Among these, we find that the transition between "winter-like" and "summer-like" polar cap N occurs one week prior to local spring equinox in the Northern Hemisphere (NH), and one week after local spring equinox in the Southern Hemisphere (SH). Thus SH polar cap N lags NH polar cap N by approximately two weeks with respect to local spring and fall equinox in each hemisphere. We show that this lag cannot be explained by differences in solar illumination alone. We also find that overall variation of N in the SH polar cap is greater than overall variation of N in the NH polar cap, except for an approximately two-month period centered on June solstice, and that the greater degree of variability of N in the SH polar cap is partly attributable to differences in illumination of the SH polar cap.

Seasonal and hemispheric asymmetries in the cold ion outflow source region: Swarm and CHAMP observations of F-region polar cap plasma density

S. M. Hatch[1*], S. Haaland[1,2], K. M. Laundal[1], T. Moretto[1], A. W. Yau[3], L. Bjoland[4], J. P. Reistad[1], A. Ohma[1], K. Oksavik[1,4]

[1]Birkeland Centre for Space Science, University of Bergen, Norway
[2]Max-Planck Institute for Solar Systems Research, Göttingen, Germany
[3]Department of Physics and Astronomy, University of Calgary, Calgary, Alberta, Canada
[4]Department of Arctic Geophysics, University Centre in Svalbard, Longyearbyen, Norway

Key Points:

- Statistics of F-region polar cap plasma density derived from 15 years of measurements exhibit several types of seasonal asymmetries
- Southern Hemisphere polar cap plasma densities lag those in Northern Hemisphere by at least two weeks around local spring and fall equinox
- Hemispheric differences in polar cap plasma density at equinoxes cannot be explained solely on the basis of differences in illumination

*Department of Physics and Technology, Allégaten 55, N-5007 Bergen, Norway

Corresponding author: S. M. Hatch, `Spencer.Hatch@uib.no`

Abstract

One of the primary mechanisms of loss of Earth's atmosphere is the persistent "cold" ($T \lesssim 20$ eV) ion outflow that has been observed in the magnetospheric lobes over large volumes with dimensions of order several Earth radii (R_E). As the main source of this cold ion outflow, the polar cap F-region ionosphere and conditions within it have a disproportionate influence on these magnetospheric regions. Using 15 years of measurements of plasma density N_e made by the Swarm spacecraft constellation and the CHAMP spacecraft within the F region of the polar cap above 80° Apex magnetic latitude, we report evidence of several types of seasonal asymmetries in polar cap N_e. Among these, we find that the transition between "winter-like" and "summer-like" polar cap N_e occurs one week prior to local spring equinox in the Northern Hemisphere (NH), and one week after local spring equinox in the Southern Hemisphere (SH). Thus SH polar cap N_e lags NH polar cap N_e by approximately two weeks with respect to local spring and fall equinox in each hemisphere. We show that this lag cannot be explained by differences in solar illumination alone. We also find that overall variation of N_e in the SH polar cap is greater than overall variation of N_e in the NH polar cap, except for an approximately two-month period centered on June solstice, and that the greater degree of variability of N_e in the SH polar cap is partly attributable to differences in illumination of the SH polar cap.

Plain Language Summary

The Earth's magnetic poles are not perfectly aligned with the Earth's geographic poles, and the degree of misalignment is greater in the Southern Hemisphere. Furthermore, as a result of the Earth's elliptical orbit around the Sun, summer and fall in the Northern Hemisphere together are approximately one week longer than summer and fall in the Southern Hemisphere, and the Earth is very slightly closer to the Sun around December solstice (summer in the Southern Hemisphere). These seasonal asymmetries, together with the asymmetric displacement of the Earth's magnetic poles relative to the geographic poles, suggest that the plasma density in the topside ionosphere's geomagnetic polar regions may also be subject to seasonal and hemispheric asymmetries. The polar regions are the primary site of loss of the Earth's atmosphere via so-called ion outflow processes that over geological time scales are believed to lead to a non-negligible loss of the Earth's atmosphere. Using 15 years of plasma density measurements made by four different satellites to statistically study the plasma density of each hemisphere's geomagnetic polar cap ionosphere in the altitude range 350–520 km, we find that the polar cap ionosphere at these altitudes exhibits a variety of seasonal and hemispheric asymmetries.

1 Introduction

A substantial fraction of the plasma in the Earth's magnetosphere is supplied by the ionosphere (e.g., Chappell et al., 1987, 2000) through ion outflow from the high-latitude polar cap regions, where terrestrial magnetic field lines are open and connected to solar wind magnetic field lines. By the same token, ion outflow is also considered to be a primary means of loss of the Earth's atmosphere (e.g., André, 2015). Ion outflow is the result of ionization of atmospheric gases and outward transport due to vertical forces. Recent results suggest that low-energy ions from the open polar cap area usually dominate the ion density and the outward flux in populating large volumes of the magnetosphere. Furthermore, ionization (i.e., availability of free charges) rather than transport is reported to be the limiting factor for ion outflow (Haaland et al., 2012; André et al., 2015).

Ionization is primarily driven by solar illumination, although other processes such as cosmic rays (e.g., Adams & Masley, 1965; Velinov, 1970) and particle precipitation also contribute (e.g., Rees, 1963, 1982). Solar radiation at ultraviolet (UV) and extreme ultraviolet (EUV) wavelengths is the most efficient in terms of ionizing atmospheric atoms and molecules and producing ion-electron pairs (e.g., S. E. Appleton, 1956; Ivanov-Kholodnyy, 1962; Rees, 1989; Brekke, 1997; Schunk & Nagy, 2009). Since the ionosphere as a whole is quasi-neutral, both the electron number density and ion number density are often simply referred to as the plasma density.

The resulting plasma density in the atmosphere is a balance between production (ionization) processes on one hand, and losses by recombination and transport processes on the other hand (e.g., Quinn & Nisbet, 1965; Khocholava, 1977; Rees, 1989; Rishbeth, 1997). Production and loss processes do not necessarily work on the same time scale, so at a given location in space, there can be significant variation in the plasma density over time.

In the terrestrial atmosphere, the peak plasma density is typically located in the ionospheric F-layers, around 200–400-km geodetic altitude (e.g., Rishbeth, 1962; Feldstein et al., 1975). Since ionization is strongly driven by solar illumination, plasma density exhibits solar cycle variations as well as strong seasonal and diurnal variations (e.g., E. V. Appleton, 1939). Typical plasma densities are of order 10^5–10^6 cm^{-3} in the sunlit ionosphere, but can be less by an order of magnitude or two in darkness.

In the polar regions the variation of plasma density with season is strongest, followed by diurnal variation and variation with solar cycle (e.g., Feldstein et al., 1975). The seasonal variation can largely be understood on the basis of solar illumination; during summer conditions, the polar cap is fully illuminated. Conversely, during winter conditions major portions of the polar cap are in complete darkness. The Sun-Earth distance plays a lesser, though non-negligible, role for variations in solar illumination (e.g., Dang et al., 2017). From the standpoint of plasma density variation, one would expect solar illumination, ionization and plasma production to be very similar in the Northern and Southern Hemisphere around equinox.

In contrast to ionization and production of ionospheric plasma, which are primarily due to solar EUV radiation, transport of ionospheric plasma is primarily driven by electromagnetic forces and organized with respect to the geomagnetic rather than the geographic poles. Horizontal transport is mainly driven by large scale magnetospheric convection set up by reconnection at the dayside magnetopause (e.g., Dungey, 1963), and thermospheric neutral winds (e.g., Förster et al., 2008). Vertical transport—upflow and outflow—is due to a combination of various forces. Theoretical descriptions of ion outflow at the polar caps were developed in the 1960s (e.g. Dessler & Michel, 1966; Nishida, 1966; Axford, 1968; Banks & Holzer, 1968) and collectively comprise the classical polar wind paradigm. In this view, light ion species in the ionosphere gain upward mobility via plasma and neutral pressure gradients as well as ambipolar electric fields formed and sustained by requiring charge balance between electrons and ions in the ionosphere. Due to the mirror force, any additional transverse acceleration near and above the exobase (500–1000 km) effectively acts as upward acceleration (e.g., Klumpar, 1979). At altitudes of a few R_E, centrifugal forces (Cladis, 1986; Horwitz et al., 1994; C. Liu et al., 1994; Nilsson et al., 2008, 2010) become dominant.

Thus, the significant difference in magnetic topology of the Northern and Southern Hemisphere polar regions (e.g., Cnossen & Förster, 2016; K. Laundal et al., 2017) is a likely factor in reported hemispheric asymmetries in ionospheric outflow around equinox (e.g., Maes et al., 2016; Haaland et al., 2017; Li et al., 2020). These differences do play a role, for example, in the seasonal variation of thermospheric and ionospheric winds (Aruliah, Farmer, Fuller-Rowell, et al., 1996; Aruliah, Farmer, Rees, & Brändström, 1996; Mikhailov & Schlegel, 2001).

Estimation of the total loss of geogenic plasma due to ion outflow is subject to additional complications that arise because the source regions (primarily the open polar cap, but also cusp and auroral zone) vary greatly in size and shape in response to solar wind driving (Sotirelis et al., 1998; Milan et al., 2008; Milan, 2009; Li et al., 2012).

In this study, we follow up on previous studies (Haaland et al., 2012; André et al., 2015; Haaland et al., 2017) indicating or otherwise suggesting that available ionospheric plasma rather than transport is the limiting factor for ion outflow. Using a large database of ionospheric plasma density measurements made by the Swarm and CHAMP satellites in both hemispheres, we seek to determine under which seasons hemispheric asymmetries in cold plasma outflow might be expected on the basis of available ionospheric plasma.

This study is organized as follows. In section 2 we describe the Swarm and CHAMP polar cap plasma density database. In section 3 we identify and describe a number of seasonal and hemispheric asymmetries in polar cap plasma density. In section 4 we consider differences in illumination and plasma production of the two polar caps using a simple model. In section 5 we discuss results from the preceding section and describe some implications for cold ion outflow. In section 6 we summarize the results of this study and conclude. We additionally describe in Appendix A–B various methodological details of this study.

2 Swarm and CHAMP Plasma Density Measurements

We use plasma density measurements made by two separate missions, the original three-satellite Swarm constellation (Friis-Christensen et al., 2008) and the Challenging Mini-Satellite Payload (CHAMP) satellite (Reigber et al., 2006).

The original three Swarm satellites complete approximately 15 orbits per day in a near-polar orbit, over the six-year period extending from launch on 22 November 2013 to the present. The two lower satellites, Swarm Alpha (Swarm A) and Swarm Charlie (Swarm C), cover the range of geodetic altitudes between 445 km and 500 km (up to 527 km during commissioning phase); Swarm Bravo (Swarm B) covers the range of geodetic altitudes between 510–545 km (down to 500 km during commissioning phase). The

Electric Field Instrument (EFI) (Knudsen et al., 2017) aboard the three original Swarm satellites includes two dedicated low-gain and high-gain Langmuir Probes (LPs). The two LPs measure plasma density and electron temperature at 2 Hz. The most complete in-flight calibrations and validations of the Swarm LP plasma density and electron temperature measurements, based on comparisons with plasma density measurements measured by other satellites and ground-based instruments, have been performed by Lomidze et al. (2018).

The CHAMP satellite also completed approximately 15 orbits per day in a near-polar orbit over a ∼10-year period extending from 15 July 2000 to 19 September 2010. The nominal range of geodetic altitudes covered by CHAMP extended over ∼300–455 km. The Planar Langmuir Probe (PLP) instrument (Rother et al., 2005) aboard CHAMP made measurements of plasma density at a 15-s cadence. In-flight calibration of the PLP instrument has been performed by McNamara et al. (2007).

In this study we use all Swarm Level 1B LP plasma density measurements downsampled to 15-s cadence, from the period between 10 Dec 2013 to 5 Feb 2020 (`https://swarm-diss.eo.esa.int/`). Downsampling is achieved by selecting every 30th measurement. We also use all CHAMP Level 2 PLP plasma density measurements from the period between 19 Feb 2002 and 21 Dec 2009 (`ftp://isdcftp.gfz-potsdam.de`) made at ≥350-km geodetic altitude. We impose this altitude restriction on CHAMP density measurements to ensure that all plasma density measurements are made above the altitude at which the $F2$-layer plasma density peak $hmF2$ is located (e.g., Shim et al., 2011; Burns et al., 2012; Bjoland et al., 2016). To Swarm plasma density measurements we also apply the Lomidze et al. (2018) in-flight calibrations (see Appendix A). Since ion outflow and ionosphere-magnetosphere coupling are organized by the geomagnetic field we are here concerned with the geomagnetic polar cap, which we define (Table 1) as the region at and above 80° magnetic latitude (MLat) in the Modified Apex coordinate system at a reference geodetic altitude of 110 km (i.e., MA_{110} coordinates) (Richmond, 1995; K. M. Laundal & Richmond, 2016). We perform the conversion of geocentric coordinates of each satellite to MA_{110} coordinates via the `apexpy` Python package (Emmert et al., 2010; van der Meeren et al., 2018). Table 1 summarizes some properties of the polar caps in each coordinate system.

Table 1. Definitions and properties of the geomagnetic and geocentric polar caps.

Hemisphere	Polar cap	Area[a] (km^2)	Circumference[a] (km)
	Geomagnetic (MA_{110}) *coordinates*		
North	$\geq 80°$ MLat[b]	3.98×10^6	7.11×10^3
South	$\leq -80°$ MLat	3.65×10^6	6.76×10^3
	Geocentric coordinates		
North	$\geq 80°$ Lat[c]	3.91×10^6	6.98×10^3
South	$\leq -80°$ Lat	3.91×10^6	6.98×10^3

[a]Area and perimeter at 0-km altitude.

[b]MLat ≡ Magnetic latitude in MA_{110} coordinates (see text).

[c]Lat ≡ Latitude in geocentric coordinates.

The total number of plasma density (N_e) measurements in the Northern Hemisphere (NH) and Southern Hemisphere (SH) geomagnetic polar caps are respectively 2,410,423 and 1,045,654. The primary reasons for the greater statistical coverage of the NH geomagnetic polar cap are that the SH geomagnetic polar cap area is approximately 9% smaller than the NH geomagnetic polar cap area (Table 1 and Figure S1 in Supporting Information), and that the relative displacement between the SH geomagnetic and geographic poles is greater compared with the NH poles. The difference in geomagnetic polar cap area arises because the Earth's magnetic field is stronger in the vicinity of the SH magnetic pole than in the vicinity of the NH magnetic pole (K. Laundal et al., 2017). The measurement coverage is approximately the same in both hemispheres (2.64 and 2.68 million measurements in the NH and SH geocentric polar caps, respectively) if one instead considers the polar caps defined in a geocentric coordinate system.

In the remainder of the manuscript all references to N_e and statistics refer only to measurements made in the geomagnetic polar caps, unless specified otherwise.

We seek to investigate seasonal and hemispheric asymmetries via statistical comparison of plasma density measurements in the geomagnetic polar cap made by different satellites. Such an investigation is complicated by a number of factors, including:

1. Differences in the altitudes of each satellite, which vary on time scales of days and years due to satellite drag and operational maneuvers, and which are systemat-

ically different in the two hemispheres due to both the shape of each satellite's orbit and the oblateness of the Earth (section A1). These differences correspond to sampling of different heights in the ionosphere.

2. Variations in solar and geomagnetic activity, which lead to differences in ionospheric conditions.

We partially account for these factors via (i) application of an empirically derived scale height to N_e measurements that "maps" N_e to a common geodetic altitude of 500 km, and (ii) application of an empirically derived correction factor that accounts for the variation of N_e measurements with 10.7-cm wavelength solar radio flux (otherwise known as the $F10.7$ index). The latter correction scales N_e to a nominal solar activity of $\langle F10.7 \rangle_{27} = 80$, where $\langle F10.7 \rangle_{27}$ is a rolling average of the preceding 27 days of the $F10.7$ index. Throughout this manuscript we use the notation N_e^* to refer to these final adjusted densities. Detailed descriptions of the derivation of the relevant scaling factors are located in Appendix A.

3 Hemispheric and Seasonal N_e^* Variations

Figure 1a shows height- and solar-flux adjusted plasma density N_e^* in the NH (blue) and SH (red) geomagnetic polar caps as a function of day of year. The transparent "x" and "+" markers respectively indicate 50,000 randomly selected individual measurements made in the NH and SH geomagnetic polar cap for each hemisphere. The solid blue and dashed red lines respectively indicate the median NH and SH N_e^* values within 10-day bins. The error bars indicate the 95% confidence interval of the median, calculated as described in Appendix B.

One of the apparent differences between the median N_e^* values in the NH and SH geomagnetic polar cap is that N_e^* takes on more extreme values in the SH than in the NH. This difference may be related to the "ionospheric annual asymmetry," which has to do with global ionospheric plasma densities around December solstice that are larger than global ionospheric plasma densities around June solstice by ~30%. This effect is well documented but not yet fully understood (e.g. Mendillo et al., 2005; Torr et al., 1980; Rishbeth & Müller-Wodarg, 2006; Lei et al., 2016; Dang et al., 2017; Xiong et al., 2018; Chartier et al., 2019); it may result from a combination of solar irradiance and photochemistry effects (Dang et al., 2017). Variation of Sun-Earth distance alone can only ac-

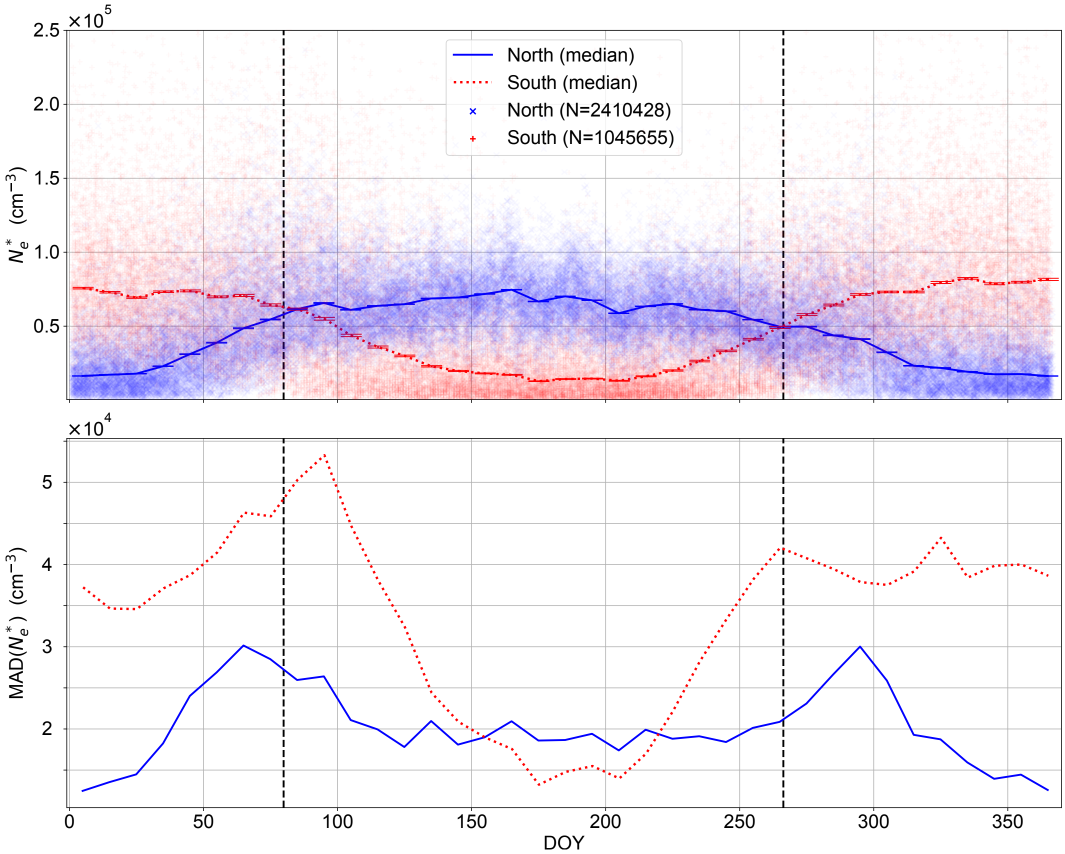

Figure 1. Swarm and CHAMP height- and solar flux-adjusted geomagnetic polar cap plasma density N_e^* statistics versus day of year in the Northern Hemisphere (solid blue line) and Southern Hemisphere (dashed red line). Here N_e^* denotes plasma density measurements that are scaled to a common geodetic altitude of 500 km and to a nominal solar activity of $\langle F10.7 \rangle_{27} = 80$, as described in Appendix A. (a) N_e^* measurements and binned medians. The transparent "x" and "+" markers respectively indicate 50,000 randomly selected individual measurements made in the NH and SH geomagnetic polar cap for each hemisphere. (Most readers will need to view the plot at full resolution or zoom in to see the distinction between these symbols.) Median N_e^* values within each 10-day bin are respectively indicated by the solid blue (North) and dashed red (South) line. Error bars indicate the 95% confidence interval of the bin median, calculated as described in Appendix B. (b) MAD(N_e^*) in the NH (solid blue line) and SH (dashed red line) geomagnetic polar caps, in 10-day bins. In both panels the dotted black lines at DOY ≈ 79.9 and DOY ≈ 266.3 respectively indicate the average DOY on which March and September equinoxes occur during the years 2000–2020; the time and date of each equinox is calculated as described in section 3. MAD≡median absolute deviation.

count for global differences of 7%, and therefore is alone insufficient to account for the observed asymmetry (Rishbeth & Müller-Wodarg, 2006).

Central tendency and variation of a statistical quantity are often indicated by the mean and standard deviation, respectively. However, N_e^* distributions in each bin in Figure 1a are heavy-tailed, and the mean is not a robust indicator of central tendency. In Figure 1a we therefore show median N_e^* statistics in each bin. Likewise, in Figure 1b we show the median absolute deviation

$$\text{MAD}(N_e^*) \equiv \text{median}\,|N_e^* - \text{median}\,(N_e^*)|$$

instead of standard deviation to indicate the variation of N_e^* in each 10-day bin. Figure 1b shows $\text{MAD}(N_e^*)$ in the Northern and Southern Hemisphere as solid blue and dashed red lines, respectively.

Two salient aspects of $\text{MAD}(N_e^*)$ curves in Figure 1b are (i) the SH $\text{MAD}(N_e^*)$ is typically greater than NH $\text{MAD}(N_e^*)$; (ii) $\text{MAD}(N_e^*)$ in the NH geomagnetic polar cap evinces two distinct peaks, before March equinox and after September equinox, while $\text{MAD}(N_e^*)$ in the SH geomagnetic polar cap evinces one primary peak after March equinox, a $\text{MAD}(N_e^*)$ "plateau" that extends from September to the end of December, and a global minimum near June solstice.

3.1 Asymmetries in seasonal variation

We now compare variations in N_e^* as a function of season. We wish to (i) avoid the systematic bias that would be introduced by performing a comparison based on day of year in the Gregorian calendar, which is inherently asymmetric from year to year with respect to the day of year on which equinoxes and solstices occur; (ii) consistently account for variation in the length of the seasons themselves, which differ on the order of days. To accomplish this, we scale the precise time period between each equinox and solstice for each year such that the period between each equinox and solstice has a duration of 1, and the total duration of all four seasons (i.e., one year) is 4. We thus define the "season parameter" $\phi_s \in [0, 4)$, with March and September equinoxes respectively corresponding to $\phi_s = 0$ and $\phi_s = 2$. June and December solstices respectively correspond to $\phi_s = 1$ and $\phi_s = 3$. The timestamps of all N_e^* measurements are then scaled to values between 0 and 4. The date and time of occurrence of each equinox and solstice

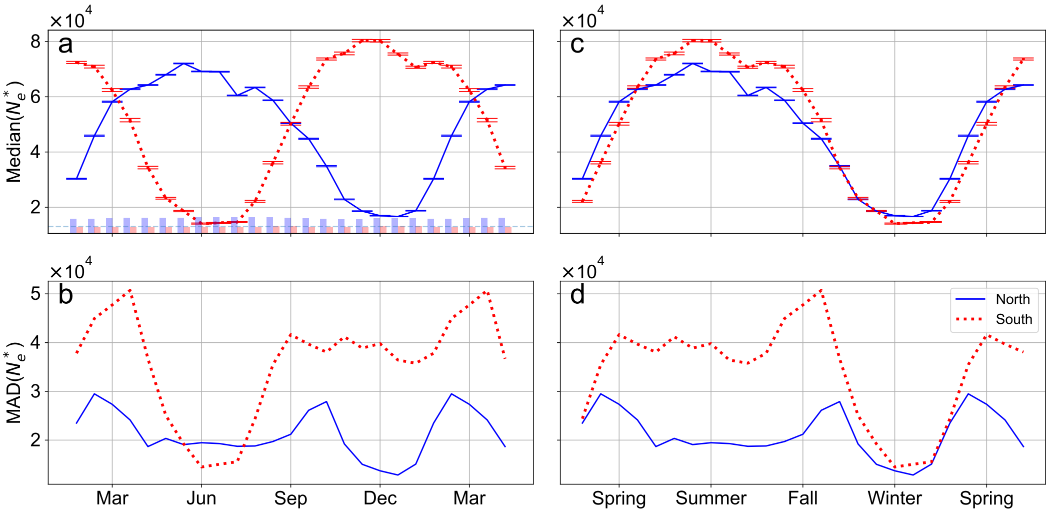

Figure 2. Median and median absolute deviation (MAD) of Swarm and CHAMP height- and solar flux-adjusted geomagnetic polar cap plasma density N_e^* statistics versus season parameter ϕ_s (see section 3.1) in the Northern Hemisphere (solid blue line) and Southern Hemisphere (dotted red line). Tick marks in each panel precisely indicate the relevant equinox or solstice. (a) Median N_e^* in each hemisphere as a function of season. (b) MAD(N_e^*) in each hemisphere as a function of season. (c) Median N_e^* in each hemisphere as a function of local season. (d) MAD(N_e^*) in each hemisphere as a function of local season. Error bars in Figures 2a and 2c indicate the 95% confidence interval of the median, calculated as described in Appendix B. The transparent histograms at the bottom of Figure 2a indicate the number of N_e^* values used to calculate the median statistic in each bin. The average number of measurements in each bin is 120,000 in the NH and 52,500 in the SH; the dashed gray line indicates $N = 54,000$. The total number of SH measurements is about 60% less than the total number of NH measurements (see section 2).

for all relevant years between 2002 and 2020 is calculated to second precision via the `skyfield` Python package (Rhodes, 2019).

Figure 2a displays median N_e^* values in the NH (solid blue line) and SH (dotted red line) geomagnetic polar caps as a function of the season parameter ϕ_s for bins of 0.2. The error bars indicate the 95% confidence interval of the median in each bin, calculated via the methodology described in Appendix B. At March equinox the median value of SH N_e^* is $7 \pm 1\%$ greater than the value of NH N_e^*, while there is apparently no such asymmetry ($0.4 \pm 1\%$) around September equinox.

Figure 2b displays MAD(N_e^*) in each hemisphere. In addition to the general trends in MAD(N_e^*) described at the beginning of this section, here it is also apparent that the combined hemispheric MAD(N_e^*) at December solstice are greater than the combined hemispheric MAD(N_e^*) around June solstice. The globally greater variability of F-region N_e^* around December solstice has been shown (Chartier et al., 2019) to result from a combination of the ionospheric annual asymmetry and O^+ plasma lifetimes that are longer during December solstice than during June solstice.

Figure 2c displays median N_e^* values in the NH (solid blue line) and SH (dotted red line) geomagnetic polar caps as a function of local season ϕ_s, where the phase of the SH ϕ_s season parameter values is shifted backward by 2 to facilitate comparison of local seasonal variations in median N_e^* for each hemisphere. From this figure it is immediately apparent that (i) the range of median SH N_e^* values in the SH is overall larger than the range of median NH N_e^* values, which is also visible in Figure 1a, and (ii) variation in median SH N_e^* lags behind median NH N_e^* around local spring and fall equinoxes by several days. We quantify this lag in the following subsection. These statistics also suggest that the annual maximum in median NH N_e^* occurs before local summer solstice, while the annual maximum in median SH N_e^* occurs at or perhaps slightly before local summer solstice. A secondary peak in median N_e^* between local summer solstice and local fall equinox is also apparent in both hemispheres.

Figure 2d displays MAD(N_e^*) in each hemisphere as a function of local season. The most immediate observation is that SH MAD(N_e^*) (dotted red line) are almost always greater than NH MAD(N_e^*) (solid blue line), except for the period between local winter and local spring where the MAD(N_e^*) values in each hemisphere are similar. Beyond this basic difference, in both hemispheres MAD(N_e^*) peaks after local fall, reaches a global minimum near local winter, and either peaks (in the NH) or plateaus (in the SH) near local spring.

3.2 Equinoctial Asymmetries

We now consider the evolution of N_e^* around equinox in each hemisphere. Figure 3a shows median NH N_e^* values relative to March equinox (thin blue line) and September equinox (thick blue line) in 15-day bins. Crossover occurs at -7.2 days relative to equinox. Figure 3b shows median SH N_e^* values relative to March equinox (thin red dotted line)

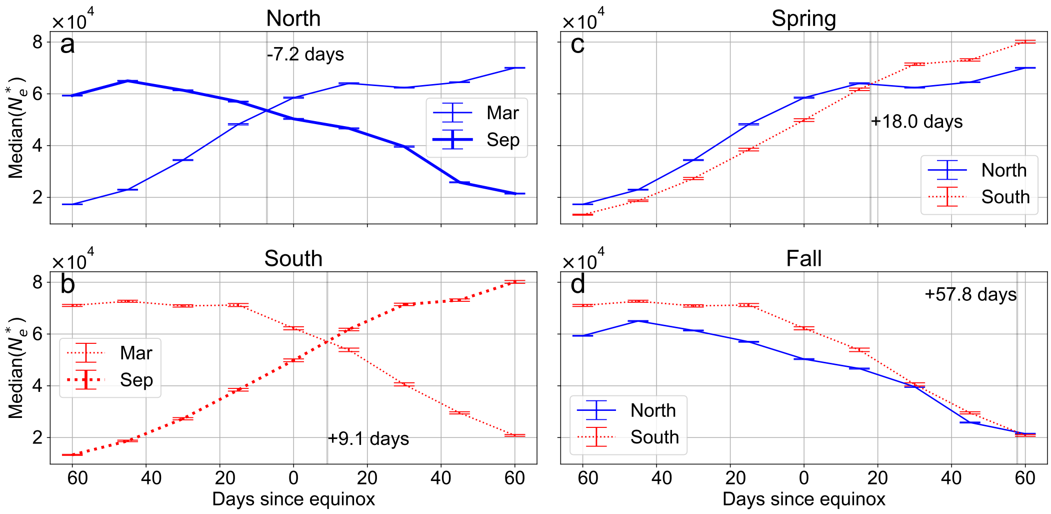

Figure 3. Median N_e^* statistics in 15-day bins relative to the number of days since equinox (Figures 3a–d). (a) Median NH N_e^* relative to March equinox (thin blue line) and September equinox (thick blue line). (b) Median SH N_e^* relative to March equinox (thin dotted red line) and September equinox (thick dotted red line). (c) Median NH N_e^* (solid blue line) and SH N_e^* (dotted red line) relative to local spring equinox. (d) Median NH N_e^* (solid blue line) and SH N_e^* (dotted red line) relative to local fall equinox. The 95% confidence intervals of the medians in 3a–d are calculated as described in Appendix B.

and September equinox (thick dotted red line). Crossover occurs at +9.1 days relative to equinox. Figure 3c shows NH and SH median N_e^* values relative to March and September equinox, respectively, and Figure 3d shows NH and SH median N_e^* values relative to September and March equinox, respectively. That is, Figure 3c and 3d show median N_e^* values in each hemisphere relative to local spring and fall, respectively.

Figure 3c shows that the local spring crossover between median NH N_e^* (solid blue line) and median SH N_e^* (dotted red line) occurs at +18 days relative to equinox. Figure 3d shows that the local fall crossover between median NH N_e^* (solid blue line) and median SH N_e^* (dotted red line) occurs at +58 days relative to equinox, but it is also apparent that these lines are very near one another over approximately +30 to +60 days after equinox. To calculate the crossover point in each panel, we interpolate between each 15-day median with a resolution of 0.1 days and determine the relative day of year for which the two lines shown in each panel are nearest each other.

4 Hemispheric and Seasonal Variations in Solar Illumination

Of the factors that influence the production of ionospheric plasma (see Introduction), solar illumination is perhaps the most important. To determine which, if any, of the asymmetries identified in the previous section can be explained purely on the basis of solar illumination, we have conducted the analysis of geomagnetic and geocentric polar cap illumination shown in Figure 4, with x axes indicating the season or local season as in Figure 2. The top row (Figures 4a–b) shows solar zenith angle χ ranges for the NH (dotted blue line and cross hatching) and SH (dotted red line and circle hatching) geomagnetic polar caps. The fourth row (Figures 4g–h) shows χ ranges for the geocentric polar caps. Gray shading in the upper half of Figures 4a–b and g–h indicates the range $\chi > \chi_m$, where, from basic trigonometry,

$$\chi_m\left(h_0\right) = \frac{\pi}{2} + \arccos\left(\frac{R}{R+h_0}\right) \tag{1}$$

is the maximum solar zenith angle at which the Sun is visible as a function of reference altitude h_0 and Earth radius R =6371 km, neglecting refraction of sunlight and the oblateness of Earth. At reference altitude h_0 =350 km, $\chi_m \approx 108.6°$.

The range of χ values for each day is produced by identifying all points on an equal-area grid in geocentric coordinates that lie within the geomagnetic polar caps (Figures 4a–b) or geocentric polar caps (Figures 4g–h). We then calculate χ at all of these points at

Figure 4. Daily average, minimum, and maximum of solar zenith angle χ (Figures 4a–b and g–h) and the plasma production model given by Equation (4) (Figures 4c–f and i–l) versus season parameter ϕ_s (season in the left panels and local season in the right panels; see section 3.1) in the Northern (blue) and Southern Hemisphere (red) geomagnetic polar caps (three upper rows, Figures 4a–f) and geocentric polar caps (three lower rows, Figures 4g–l). Tick marks in each panel precisely indicate the relevant equinox or solstice. The average (panels a–d and g–j) or standard deviation (panels e–f and k–l) of each quantity is indicated by a thick dotted line (NH) and thin dotted line (SH). The average plus or minus one standard deviation in panels a–d and g–j is indicated by cross and circle hatching for the Northern and Southern Hemisphere, respectively. The gray shading in the upper half of panels a–b and e–f indicates the range of χ values above the maximum solar zenith angle χ_m (χ_m 108.6°) at which the Sun is visible at 350-km altitude according to Equation (1). The solid blue (NH) and red (SH) lines in Figures 4c–f are median geomagnetic polar cap N_e^* (Figures 4c–d) and MAD(N_e^*) (Figures 4e–f), taken and scaled from Figures 2a–d. The corresponding lines in Figures 4i–l are median geocentric polar cap N_e^* (Figures 4i–j) and MAD(N_e^*) (Figures 4k–l).

5 Discussion

Results in the preceding sections indicate the existence of several seasonal and hemispheric asymmetries in the plasma density of the geomagnetic polar caps. Table 2 summarizes the equinoctial asymmetries identi ed from Figures 1{3 on the basis of the combined database of Swarm and CHAMP measurements.

The most signi cant results of analysis in section 3 are displayed in Figure 3. In Figure 3a the crossover point of the two Northern Hemisphere (solid blue) lines occurs approximately 7 days before equinox, whereas in Figure 3b the crossover point of the two Southern Hemisphere (dotted red) lines occurs approximately 9.1 days after equinox. Thus the days on which the local hemisphere geomagnetic polar cap density N_e crossover near local equinox occurs are hemispherically asymmetric. This asymmetry is also present when the polar caps are de ned in geocentric coordinates (not shown), and so is not the result of a particular choice of coordinate system.

Comparison of median N_e curves from each geomagnetic polar cap around local spring (Figure 3c) and around local fall (Figure 3d) shows that the crossover points in both hemispheres occur more than two weeks after equinox. This suggests the existence of a seasonal \phase o set" between the two hemispheres in median N_e around local spring and fall equinoxes, whereby N_e in the SH geomagnetic polar cap lags N_e in the NH geomagnetic polar cap by at least two weeks. Median N_e curves from each geocentric polar cap around local spring equinox (Figure 4j) exhibit a similar, even more pronounced lag, whereby N_e in the SH geocentric polar cap lags N_e in the NH geocentric polar cap by six weeks or more.

Thus the relative lag between SH and NH polar cap N_e around local spring equinox is not the result of choosing a particular de nition of the polar caps (i.e., geomagnetic or geocentric polar caps; see Table 2). On the other hand there is apparently no lag between SH and NH geocentric polar cap N_e around local fall equinox, which suggests that the relative lag exhibited by N_e in the geomagnetic polar caps is related to the choice of coordinate system (i.e., geomagnetic instead of geocentric polar caps). The di erent lags imply that there are at least two contributing factors to the delay, which likely operate somewhat di erently in the two sets of polar caps during local spring and local fall. Here it is worth noting that the existence of a relative lag in geomagnetic polar cap N_e around local fall equinox may be related to reported hemispheric asymmetry in ion out-

outflow processes and ionosphere-magnetosphere coupling that is organized by the geomagnetic field (Haaland et al., 2012; André et al., 2015; Haaland et al., 2017).

To test the robustness of the asymmetries identified in Figures 1–3 and Table 1, we have also performed the analysis separately for each of the four satellites used in this study (not shown). The values obtained from each of these separate analyses are shown in the rightmost column of Table 2. All of the asymmetries we have just discussed also appear in the analyses based on measurements from individual satellites. More specifically with the exception of the weak evidence for a NH/SH crossover delay at September equinox, the other delays are consistent between all four spacecraft albeit with slight differences in the estimated Δt values.

We believe these separate analyses are important indicators of the robustness of each asymmetry, since the Swarm and CHAMP satellites monitor polar cap plasma density at effectively three different altitude ranges over two different portions of a solar cycle, with two different and independent types of Langmuir probe instruments and three different orbits.

To understand whether these observed asymmetries can be explained solely on the basis of differences in solar illumination, in section 4 we have used an illumination-dependent plasma production model with representative values of parameters such as neutral temperature and absorption cross section. More significant than any of the chosen values of these neutral atmosphere parameters, however, is our much more basic (and unrealistic) assumption of a neutral atmosphere that consists of a single species, a single wavelength-independent absorption cross section, and a constant temperature profile that does not vary with season.

One purpose of this study is to determine whether the hemispheric asymmetry in magnetospheric lobe cold plasma density reported by Haaland et al. (2017) could be explained on the basis of plasma densities in the ionospheric polar caps. In specific, they found that the distribution of densities in the NH lobe were overall greater than the distribution of densities in the SH lobe around September equinox, and speculated whether this asymmetry was due to differences in outflow and plasma densities between NH and SH. No such corresponding asymmetry in median geomagnetic polar cap N_e at September equinox is apparent in Figures 1a and 2a. There is, however, evidence of a corresponding asymmetry in the median geographic polar cap N_e (Figure 4i).

when all three satellites flew at approximately 500-km geodetic altitude in the NH (520-km geodetic altitude in the SH). The orbit of Swarm B was later boosted to higher altitudes, while the orbits of Swarm A and Swarm C were lowered. (The altitude distribution covered by Swarm A is not shown since it and Swarm C have followed very similar orbital trajectories since launch.)

Comparison of the geodetic altitude distributions in each hemisphere indicates a systematic difference in each satellite's range of altitudes: in each case the NH geomagnetic polar cap distribution of altitudes is systematically offset by approximately 20 km relative to the SH geomagnetic polar cap distribution. This is due to the combined effects of the Earth's oblateness and the slightly elliptical orbit of each satellite.

From 380 conjunctions between Swarm B and either Swarm A or Swarm C for which Swarm LP data is currently available (Dec 2013 through Feb 2020) we derive an empirical scale height. These conjunctions were identified via the Query tool (`https://sscweb.gsfc.nasa.gov/cgi-bin/Query.cgi`) at NASA's Satellite Situation Center Web (`https://sscweb.gsfc.nasa.gov/`) by requiring a horizontal separation of less than 100 km after radially tracing the footpoint of each satellite to a common altitude.

For each conjunction identified by the Query tool, we use a 10-minute window to calculate the time at which the angular separation

$$\Delta\zeta = \arccos\left[\sin\lambda_1^m \sin\lambda_2^m + \cos\lambda_1^m \cos\lambda_2^m \cos\left(\mid \theta_1 - \theta_2 \mid\right)\right], \qquad \text{(A2)}$$

between the two satellites is a minimum. Here λ^m and θ respectively denote MLat and geomagnetic longitude in MA_{110} coordinates. We then use this more precise list of conjunction times to calculate the Vertical Scale Height VSH $\equiv dh/(d\ln N_e)$ (e.g., Hu et al., 2019).

Each conjunction corresponds to a single point in Figure A1c, which shows the logarithm of the ratio of N_e measurements made by Swarm B and either Swarm A or Swarm C on the x axis, and the altitude separation Δh in kilometers between the satellite pair on the y axis. The circle and star markers respectively denote dayside (6–18 MLT) and nightside (18–6 MLT) conjunctions. The spread in the logarithm of density ratios on the x axis indicate overall significant variability in the plasma density at each altitude. This spread is not surprising given the various contributions to density made by, for example, plasma convection, polar cap patches, and auroral precipitation. On the other hand, individual points in Figure A1c also indicate the existence of a particular scale height, or an approximately linear relationship between altitude difference and the logarithm of the ratio of plasma density at each altitude.

We use so-called "robust regression" to estimate the VSH from measurements in Figure A1c. In specific we perform an iterative Huber-weighted least-squares linear regression (e.g., Huber (1973); Holland and Welsch (1977)) to data in Figure A1c with the function

$$\log\left(N_e^{\mathrm{A,C}}/N_e^{\mathrm{B}}\right) = \beta\Delta h, \tag{A3}$$

where $\beta \equiv 1/\mathrm{VSH}$. We use the `HuberRegressor` module of the `Scikit-learn` Python package (Pedregosa et al., 2011) with $\epsilon = 1.5$. The ϵ parameter in Huber-weighted iterative regression controls the degree to which the regression is sensitive to outlier points.

From this regression we obtain the purple and brown lines, which respectively correspond to VSH= 205 km on the "dayside" and VSH= 167 km on the "nightside." We use magnetic local time (MLT) in MA_{110} coordinates to define "dayside" as $6 \leq \mathrm{MLT} < 18$, and "nightside" as $\mathrm{MLT} < 6$ and $\mathrm{MLT} \geq 18$. These VSH values are within the range of typical estimates at geodetic altitudes of 350–500 km (see, e.g., Figure 2 in Hu et al. (2019) and Figure 1B in Stankov and Jakowski (2006)). To each N_e measurement we then apply a scaling factor

$$N_{e,h_0} = N_e \exp\left[\left(h - h_0\right)/\mathrm{VSH}\right], \tag{A4}$$

where h is the altitude at which the measurement is made and VSH is the empirical scale height. We arbitrarily select a reference geodetic altitude $h_0 = 500$ km. This scaling decreases the value of N_e for measurements made below h_0 and increases the value of N_e for measurements made above h_0.

A2 Adjustment of N_e for $F10.7$ Variations

In addition to variation with altitude, polar cap N_e also varies with the intensity of sunlight. We use an average of the $F10.7$ index during the preceding 27 days, denoted by $\langle F10.7\rangle_{27}$, as a proxy for solar EUV intensity. (The $F10.7$ index is publically available via the NASA OMNI database at `https://omniweb.gsfc.nasa.gov/form/dx1.html`.) Another common choice for averaging the $F10.7$ index is a centered 81-day window (e.g., L. Liu & Chen, 2009; Schunk & Nagy, 2009). We have elected to use $\langle F10.7\rangle_{27}$ instead,

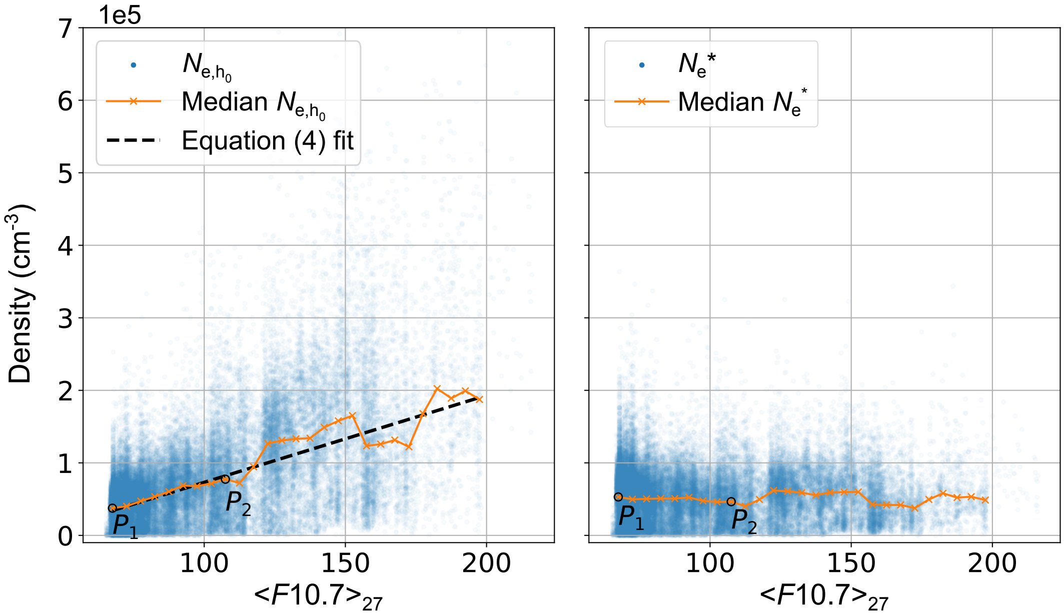

Figure A2. Height-scaled plasma densities before (left) and after (right) adjusting for variation in $\langle F10.7\rangle_{27}$ using Equation (A6). In the left panel the black dashed line indicates the model given by Equation (A5) with best-fit parameters a = 0.02564 and N = 46,780 obtained by performing the iterative Huber-weighted least-squares nonlinear regression described in the text. The two points P_1 and P_2 indicate the two points used to obtain initial estimates for model parameters a and N, and are shown in the right panel to indicate the effect of applying Equation (A6) to N_{e,h_0} values. In both panels the orange line indicates the median value, N_{e,h_0} in the left panel and N_e^{adj} in the right panel, within $\langle F10.7\rangle_{27}$ bins of 5.

since we find that the RMS error between $\langle F10.7\rangle_{27}$ and N_{e,h_0} is slightly (∼5%) lower than the RMS error between an 81-day centered average of the $F10.7$ index and N_{e,h_0}.

Figure A2a shows height-scaled polar cap N_{e,h_0} plotted versus $\langle F10.7\rangle_{27}$. The orange line indicates median N_{e,h_0} values within bins of 5 for $\langle F10.7\rangle_{27}$ between 65 and 200. The variation of median N_{e,h_0} with $\langle F10.7\rangle_{27}$ is approximately linear.

To scale N_{e,h_0} measurements for variation with $F10.7$, we perform an iterative Huber-weighted least-squares linear regression to all 3,456,077 N_{e,h_0} values with a model of the form

$$N_{e,h_0} = A\langle F10.7\rangle_{27} - B = N\left(a\langle F10.7\rangle_{27} - 1\right). \tag{A5}$$

In practice the actual best-fit parameters are not sensitive to our choice of initial parameter estimates, but for illustrative purposes we use the two points indicated in Figure A2a, $P_1 = (F_1, N_1) = (67.5, 37516)$ and $P_2 = (F_2, N_2) = (107.5, 77460)$ together with the model in Equation (A5) to obtain the initial model estimates $\hat{A} = (N_2 - N_1)/(F_2 - F_1) = 999$ and $\hat{B} = \hat{N} = \hat{A}F_1 - N_1 = 29890$, such that $\hat{a} = \hat{A}/\hat{B} = 0.033$.

The resulting best-fit model parameters with weighting parameter $\epsilon = 1.5$ are $a = 0.02564$ and $N = 46,780$; the resulting model of the form given by Equation (A5) is indicated by the black dashed line in Figure A2a. These fit parameters are obtained by requiring that the relative change in each model parameter be less than 10^{-8} after each iteration, which is generally acheived after 35–60 iterations. We apply the portion of the model in Equation (A5) that is dependent on $\langle F10.7\rangle_{27}$, namely the parameter a, to each N_{e,h_0} value to finally obtain the height- and solar flux-adjusted density

$$N_e^* = N_{e,h_0}\frac{80a - 1}{a\langle F10.7\rangle_{27} - 1}. \tag{A6}$$

The numerator in Equation (A6) scales the final adjusted density N_e to a nominal solar flux level of $\langle F10.7\rangle_{27} = 80$. These final adjusted densities are shown in Figure A2b.

Appendix B 95% Confidence Interval of the Median

The 95% confidence interval of each median displayed in Figure 1a is calculated in each DOY bin by first sorting the N_e^* values in that DOY bin, and then identifying the value of N_e^* corresponding to the Lth and Uth sorted sample in that DOY bin. These sorted sample numbers are given by (Conover, 1999)

$$L = \lfloor Q_b(0.025, N, 0.5) \rfloor;$$
$$U = \lceil Q_b(0.975, N, 0.5) \rceil; \tag{B1}$$

where $\lfloor\rfloor$ and $\lceil\rceil$ are respectively floor and ceiling functions and $Q_b(p, N, q)$ is the quantile function, otherwise known as the "inverse cumulative distribution" or "percent-point function," of the binomial distribution. The parameters of this quantile function are the probability p, the number of observations N, and the quantile of interest q. We use $p =$ 0.025, 0.975 corresponding to the 95% confidence interval, and $q = 0.5$ corresponding to the 50% quantile or median. We calculate $Q_b(p, N, q)$ via the `stats.binom.ppf` method of the `scipy` Python package (Virtanen et al., 2020).

Acknowledgments

Work at the Birkeland Center for Space Science and the University of Bergen was funded by the Research Council of Norway/CoE under contract 223252/F50 and by ESA contract 4000126731 in the framework of EO Science for Society.

The Level 2 CHAMP PLP dataset and Level 1B Swarm LP dataset are publically accessible via `ftp://isdcftp.gfz-potsdam.de` and `https://swarm-diss.eo.esa.int/`, respectively. The $F10.7$ index is available via the NASA OMNI database (`https://omniweb.gsfc.nasa.gov/form/dx1.html`)

References

Adams, G. W., & Masley, A. J. (1965, Mar). Production rates and electron densities in the lower ionosphere due to solar cosmic rays. *Journal of Atmospheric and Terrestrial Physics*, *27*(3), 289-298. doi: 10.1016/0021-9169(65)90029-2

André, M. (2015, Dec). Previously hidden low-energy ions: a better map of near-Earth space and the terrestrial mass balance. *Physica Scripta*, *90*(12), 128005. doi: 10.1088/0031-8949/90/12/128005

André, M., Li, K., & Eriksson, A. I. (2015, Feb). Outflow of low-energy ions and the solar cycle. *Journal of Geophysical Research (Space Physics)*, *120*(2), 1072-1085. doi: 10.1002/2014JA020714

Appleton, E. V. (1939, July). Characteristic variation of region f_2 ionization throughout the year. *Nature*, *144*(3638), 151-152. doi: 10.1038/144151a0

Appleton, S. E. (1956, Jan). Regularities and irregularities in the ionosphere. *Vistas in Astronomy*, *2*(1), 779-790. doi: 10.1016/0083-6656(56)90001-0

Aruliah, A. L., Farmer, A. D., Fuller-Rowell, T. J., Wild, M. N., Hapgood, M., & Rees, D. (1996, July). An equinoctial asymmetry in the high-latitude thermosphere and ionosphere. *jgr*, *101*, 15713-15722. doi: 10.1029/95JA01102

Aruliah, A. L., Farmer, A. D., Rees, D., & Brändström, U. (1996, July). The seasonal behavior of high-latitude thermospheric winds and ion velocities observed over one solar cycle. *Journal of Geophysical Research: Space Physics*, *101*, 15701-15712. doi: 10.1029/96JA00360

Axford, W. I. (1968, November). The polar wind and the terrestrial helium budget. *J. Geophys. Res.*, *73*, 6855-6859. doi: 10.1029/JA073i021p06855

Banks, P. M., & Holzer, T. E. (1968). The polar wind. *Journal of Geophysical Research*, *73*(21), 6846–6854. doi: 10.1029/JA073i021p06846

Bjoland, L. M., Belyey, V., Løvhaug, U. P., & La Hoz, C. (2016, sep). An evaluation of International Reference Ionosphere electron density in the polar cap and cusp using EISCAT Svalbard radar measurements. *Ann. Geophys.*, *34*(9), 751–758. doi: 10.5194/angeo-34-751-2016

Brekke, A. (1997). *Physics of the polar upper atmosphere*. Springer Nature.

Burns, A. G., Solomon, S. C., Wang, W., Qian, L., Zhang, Y., & Paxton, L. J. (2012, sep). Daytime climatology of ionospheric N m F 2 and h m F 2 from COSMIC data. *Journal of Geophysical Research: Space Physics*, *117*(A9). doi: 10.1029/2012JA017529

Chapman, S. (1931, jan). The absorption and dissociative or ionizing effect of monochromatic radiation in an atmosphere on a rotating earth. *Proceedings of the Physical Society*, *43*(1), 26–45. doi: 10.1088/0959-5309/43/1/305

Chappell, C. R., Giles, B. L., Moore, T. E., Delcourt, D. C., Craven, P. D., & Chandler, M. O. (2000, April). The adequacy of the ionospheric source in supplying magnetospheric plasma. *Journal of Atmospheric and Solar-Terrestrial Physics*, *62*, 421-436. doi: 10.1016/S1364-6826(00)00021-3

Chappell, C. R., Moore, T. E., & Waite, J. H., Jr. (1987, June). The ionosphere as a fully adequate source of plasma for the earth's magnetosphere. *J. Geophys. Res.*, *92*, 5896-5910. doi: 10.1029/JA092iA06p05896

Chartier, A. T., Huba, J. D., & Mitchell, C. N. (2019, nov). On the Annual Asymmetry of High-Latitude Sporadic F. *Space Weather*, *17*(11), 1618–1626. doi: 10.1029/2019SW002305

Cladis, J. B. (1986, September). Parallel acceleration and transport of ions from polar ionosphere to plasma sheet. *Geophys. Res. Letters*, *13*, 893-896. doi: 10.1029/GL013i009p00893

Cnossen, I., & Förster, M. (2016, January). North-south asymmetries in the polar thermosphere-ionosphere system: Solar cycle and seasonal influences. *Journal of Geophysical Research (Space Physics)*, *121*, 612-627. doi: 10.1002/2015JA021750

Conover, W. J. (1999). *Practical Nonparametric Statistics* (3rd ed.). John Wiley & Sons.

Dang, T., Wang, W., Burns, A., Dou, X., Wan, W., & Lei, J. (2017, jun). Simulations of the ionospheric annual asymmetry: Sun-Earth distance effect. *Journal of Geophysical Research: Space Physics*, *122*(6), 6727–6736. doi: 10.1002/2017JA024188

Dessler, A. J., & Michel, F. C. (1966, Mar). Plasma in the geomagnetic tail. *Journal of Geophysical Research: Space Physics*, *71*(5), 1421-1426. doi: 10.1029/JZ071i005p01421

Dungey, J. W. (1963, Jan). Interactions of solar plasma with the geomagnetic field. *Planetary and Space Science*, *10*, 233-237. doi: 10.1016/0032-0633(63)90020-5

Emmert, J. T., Richmond, A. D., & Drob, D. P. (2010, aug). A computationally compact representation of Magnetic-Apex and Quasi-Dipole coordinates with smooth base vectors. *Journal of Geophysical Research: Space Physics*, *115*(A8). doi: 10.1029/2010JA015326

Feldstein, I. I., Lyatskaya, A. M., Sumaruk, P. V., & Shevnina, N. F. (1975, Dec). Ionization of the F-layer of the ionosphere and variations of the magnetic field in the near-polar region. *Geomagnetism and Aeronomy*, *15*, 1021-1027.

Fennelly, J., & Torr, D. (1992, jul). Photoionization and photoabsorption cross sections of O, N2, O2, and N for aeronomic calculations. *Atomic Data and Nuclear Data Tables*, *51*(2), 321–363. doi: 10.1016/0092-640X(92)90004-2

Förster, M., Rentz, S., Köhler, W., Liu, H., & Haaland, S. E. (2008). IMF dependence of high-latitude thermospheric wind pattern derived from CHAMP cross-track measurements. *Annales Geophysicae*, *26*(6), 1581–1595. doi: 10.5194/angeo-26-1581-2008

Friis-Christensen, E., Lühr, H., Knudsen, D., & Haagmans, R. (2008, jan). Swarm – An Earth Observation Mission investigating Geospace. *Advances in Space Research*, *41*(1), 210–216. doi: 10.1016/j.asr.2006.10.008

Haaland, S., Lybekk, B., Maes, L., Laundal, K., Pedersen, A., Tenfjord, P., ... Snekvik, K. (2017, January). North-south asymmetries in cold plasma density in the magnetotail lobes: Cluster observations. *Journal of Geophysical Research: Space Physics*, *122*, 136-149. doi: 10.1002/2016JA023404

Haaland, S., Svenes, K., Lybekk, B., & Pedersen, A. (2012, Jan). A survey of the polar cap density based on Cluster EFW probe measurements: Solar wind and solar irradiation dependence. *Journal of Geophysical Research (Space Physics)*, *117*(A1), A01216. doi: 10.1029/2011JA017250

Holland, P. W., & Welsch, R. E. (1977, jan). Robust regression using iteratively reweighted least-squares. *Communications in Statistics - Theory and Methods*, *6*(9), 813–827. doi: 10.1080/03610927708827533

Horwitz, J. L., Ho, C. W., Scarbro, H. D., Wilson, G. R., & Moore, T. E. (1994). Centrifugal acceleration of the polar wind. *Journal of Geophysical Research*, *99*(A8), 15051. doi: 10.1029/94JA00924

Hu, A., Carter, B., Currie, J., Norman, R., Wu, S., Wang, X., & Zhang, K. (2019, jun). Modeling of Topside Ionospheric Vertical Scale Height Based on Ionospheric Radio Occultation Measurements. *Journal of Geophysical Research: Space Physics*, *124*(6), 4926–4942. doi: 10.1029/2018JA026280

Huber, P. J. (1973, sep). Robust Regression: Asymptotics, Conjectures and Monte Carlo. *The Annals of Statistics*, *1*(5), 799–821. doi: 10.1214/aos/1176342503

Huestis, D. L. (2001). Accurate evaluation of the Chapman function for atmospheric attenuation. *Journal of Quantitative Spectroscopy and Radiative Transfer*, *69*(6), 709–721. doi: 10.1016/S0022-4073(00)00107-2

Ieda, A., Oyama, S., Vanhamäki, H., Fujii, R., Nakamizo, A., Amm, O., ... Nishitani, N. (2014, dec). Approximate forms of daytime ionospheric conductance. *Journal of Geophysical Research: Space Physics*, *119*(12), 10,310–397,415. doi: 10.1002/2014JA020665

Ivanov-Kholodnyy, G. S. (1962, Jan). Ionization of the Upper Atmosphere by Solar

Short-Wave Radiation. *Geomagnetism and Aeronomy*, *2*, 561.

Khocholava, G. M. (1977, Mar). On diffusion-recombination parameters in the F-region of the ionosphere. *Journal of Atmospheric and Terrestrial Physics*, *39*, 389-391. doi: 10.1016/S0021-9169(77)90154-4

Klumpar, D. M. (1979, Aug). Transversely accelerated ions: An ionospheric source of hot magnetospheric ions. *Journal of Geophysical Research: Space Physics*, *84*(A8), 4229-4237. doi: 10.1029/JA084iA08p04229

Knudsen, D. J., Burchill, J. K., Buchert, S. C., Eriksson, A. I., Gill, R., Wahlund, J., ... Moffat, B. (2017, feb). Thermal ion imagers and Langmuir probes in the Swarm electric field instruments. *Journal of Geophysical Research: Space Physics*, *122*(2), 2655–2673. doi: 10.1002/2016JA022571

Laundal, K., Cnossen, I., Milan, S. E., Haaland, S. E., Coxon, J., Pedatella, N. M., ... Reistad, J. P. (2017). North-South asymmetries in Earth's magnetic field - Effects on high-latitude geospace. *Space Sci. Reviews.*, *193*.

Laundal, K. M., & Richmond, A. D. (2016). Magnetic Coordinate Systems. *Space Science Reviews*, 1–33. doi: 10.1007/s11214-016-0275-y

Lei, J., Wang, W., Burns, A. G., Luan, X., & Dou, X. (2016, jul). Can atomic oxygen production explain the ionospheric annual asymmetry? *Journal of Geophysical Research: Space Physics*, *121*(7), 7238–7244. doi: 10.1002/2016JA022648

Li, K., Förster, M., Rong, Z., Haaland, S., Kronberg, E., Cui, J., ... Wei, Y. (2020, mar). The Polar Wind Modulated by the Spatial Inhomogeneity of the Strength of the Earth's Magnetic Field. *Journal of Geophysical Research: Space Physics*, e2020JA027802. doi: 10.1029/2020JA027802

Li, K., Haaland, S., Eriksson, A., André, M., Engwall, E., Wei, Y., ... Ren, Q. Y. (2012, Sep). On the ionospheric source region of cold ion outflow. *Geophysical Research Letters*, *39*(18), L18102. doi: 10.1029/2012GL053297

Liu, C., Perez, J. D., Moore, T. E., & Chappell, C. R. (1994, feb). Low energy particle signature of substorm dipolarization. *Geophysical Research Letters*, *21*(3), 229–232. doi: 10.1029/93GL02839

Liu, L., & Chen, Y. (2009, oct). Statistical analysis of solar activity variations of total electron content derived at Jet Propulsion Laboratory from GPS observations. *Journal of Geophysical Research: Space Physics*, *114*(A10). doi:

10.1029/2009JA014533

Lomidze, L., Knudsen, D. J., Burchill, J., Kouznetsov, A., & Buchert, S. C. (2018). Calibration and validation of Swarm plasma densities and electron temperatures using ground-based radars and satellite radio occultation measurements. *Radio Science*, *53*(1), 15–36. doi: 10.1002/2017RS006415

Maes, L., Maggiolo, R., & De Keyser, J. (2016). Seasonal variations and north-south asymmetries in polar wind outflow due to solar illumination. *Ann. Geophys.*, *34*, 961-974. doi: doi:10.5194/angeo-34-961-2016

McNamara, L. F., Cooke, D. L., Valladares, C. E., & Reinisch, B. W. (2007, apr). Comparison of CHAMP and Digisonde plasma frequencies at Jicamarca, Peru. *Radio Science*, *42*(2). doi: 10.1029/2006RS003491

Mendillo, M., Huang, C.-L., Pi, X., Rishbeth, H., & Meier, R. (2005, oct). The global ionospheric asymmetry in total electron content. *Journal of Atmospheric and Solar-Terrestrial Physics*, *67*(15), 1377–1387. doi: 10.1016/j.jastp.2005.06.021

Mikhailov, A. V., & Schlegel, K. (2001). Equinoctial transitions in the ionosphere and thermosphere. *Annales Geophysicæ*, *19*, 783-796. doi: 10.5194/angeo-19-783-2001

Milan, S. E. (2009, Sep). Both solar wind-magnetosphere coupling and ring current intensity control of the size of the auroral oval. *Geophysical Research Letters*, *36*(18), L18101. doi: 10.1029/2009GL039997

Milan, S. E., Boakes, P. D., & Hubert, B. (2008, Sep). Response of the expanding/contracting polar cap to weak and strong solar wind driving: Implications for substorm onset. *Journal of Geophysical Research (Space Physics)*, *113*(A9), A09215. doi: 10.1029/2008JA013340

Nilsson, H., Engwall, E., Eriksson, A., Puhl-Quinn, P. A., & Arvelius, S. (2010, February). Centrifugal acceleration in the magnetotail lobes. *Annales Geophysicae*, *28*, 569-576. doi: 10.5194/angeo-28-569-2010

Nilsson, H., Waara, M., Marghitu, O., Yamauchi, M., Lundin, R., Rème, H., … Korth, A. (2008, February). An assessment of the role of the centrifugal acceleration mechanism in high altitude polar cap oxygen ion outflow. *Annales Geophysicae*, *26*, 145-157. doi: 10.5194/angeo-26-145-2008

Nishida, A. (1966, dec). Formation of plasmapause, or magnetospheric plasma knee, by the combined action of magnetospheric convection and plasma escape from the tail. *Journal of Geophysical Research*, *71*(23), 5669–5679. doi: 10.1029/JZ071i023p05669

Pedregosa, F., Varoquaux, G., Gramfort, A., Michel, V., Thirion, B., Grisel, O., ... Duchesnay, E. (2011). Scikit-learn: Machine learning in Python. *Journal of Machine Learning Research*, *12*, 2825–2830.

Quinn, T. P., & Nisbet, J. S. (1965, Jan). Recombination and Transport in the Nighttime F Layer of the Ionosphere. *Journal of Geophysical Research: Space Physics*, *70*(1), 113-130. doi: 10.1029/JZ070i001p00113

Rees, M. H. (1963, Oct). Auroral ionization and excitation by incident energetic electrons. *Planetary and Space Science*, *11*(10), 1209-1218. doi: 10.1016/0032-0633(63)90252-6

Rees, M. H. (1982, May). On the interaction of auroral protons with the earth's atmosphere. *Planetary and Space Science*, *30*(5), 463-472. doi: 10.1016/0032-0633(82)90056-3

Rees, M. H. (1989). *Physics and chemistry of the upper atmosphere.* Cambridge, United Kingdom: Cambridge University Press.

Reigber, C., Lühr, H., Grunwaldt, L., Förste, C., König, R., Massmann, H., & Falck, C. (2006). CHAMP Mission 5 Years in Orbit. In *Observation of the earth system from space* (pp. 3–15). Berlin/Heidelberg: Springer-Verlag. doi: 10.1007/3-540-29522-4_1

Rhodes, B. (2019, Jul). *Skyfield: High precision research-grade positions for planets and Earth satellites generator.*

Richmond, A. D. (1995). Ionospheric Electrodynamics Using Magnetic Apex Coordinates. *Journal of geomagnetism and geoelectricity*, *47*(2), 191–212. doi: 10.5636/jgg.47.191

Rishbeth, H. (1962, Apr). Atmospheric composition and the F layer of the ionosphere. *Planetary and Space Science*, *9*(4), 149-152. doi: 10.1016/0032-0633(62)90002-8

Rishbeth, H. (1997, Oct). The ionospheric E-layer and F-layer dynamos - a tutorial review. *Journal of Atmospheric and Solar-Terrestrial Physics*, *59*, 1873-1880. doi: 10.1016/S1364-6826(97)00005-9

Rishbeth, H., & Müller-Wodarg, I. C. F. (2006, dec). Why is there more ionosphere in January than in July? The annual asymmetry in the F2-layer. *Annales Geophysicae*, *24*(12), 3293–3311. doi: 10.5194/angeo-24-3293-2006

Rother, M., Choi, S., Mai, W., Lühr, H., & Cooke, D. (2005, jan). Status of the CHAMP ME data processing. In *Earth observation with champ results from three years in orbit* (p. 413). doi: 10.1007/3-540-26800-6_66

Schunk, R., & Nagy, A. (2009). *Ionospheres* (Second ed.). Cambridge: Cambridge University Press. doi: 10.1017/CBO9780511635342

Shim, J. S., Kuznetsova, M., Rastätter, L., Hesse, M., Bilitza, D., Butala, M., … Rideout, B. (2011, dec). CEDAR Electrodynamics Thermosphere Ionosphere (ETI) Challenge for systematic assessment of ionosphere/thermosphere models: NmF2, hmF2, and vertical drift using ground-based observations. *Space Weather*, *9*(12). doi: 10.1029/2011SW000727

Sotirelis, T., Newell, P. T., & Meng, C. (1998, January). Shape of the open-closed boundary of the polar cap as determined from observations of precipitating particles by up to four DMSP satellites. *Journal of Geophysical Research: Space Physics*, *103*, 399-406. doi: 10.1029/97JA02437

Stankov, S., & Jakowski, N. (2006, jan). Topside ionospheric scale height analysis and modelling based on radio occultation measurements. *Journal of Atmospheric and Solar-Terrestrial Physics*, *68*(2), 134–162. doi: 10.1016/j.jastp.2005.10.003

Torr, D. G., Torr, M. R., & Richards, P. G. (1980, may). Causes of the F region winter anomaly. *Geophysical Research Letters*, *7*(5), 301–304. doi: 10.1029/GL007i005p00301

van der Meeren, C., Burrell, A. G., & Laundal, K. M. (2018). *apexpy: Apexpy version 1.0.3.* http://doi.org/10.5281/zenodo.1214207.

Velinov, P. (1970, Feb). Solar cosmic ray ionization in the low ionosphere. *Journal of Atmospheric and Terrestrial Physics*, *32*, 139-147. doi: 10.1016/0021-9169(70)90187-X

Virtanen, P., Gommers, R., Oliphant, T. E., Haberland, M., Reddy, T., Cournapeau, D., … Contributors, S. . . (2020). SciPy 1.0: Fundamental Algorithms for Scientific Computing in Python. *Nature Methods*. doi: https://doi.org/10.1038/s41592-019-0686-2

Xiong, C., Stolle, C., & Park, J. (2018, apr). Climatology of GPS signal loss ob-

served by Swarm satellites. *Ann. Geophys.*, *36*(2), 679–693. doi: 10.5194/angeo
-36-679-2018